

## Extended Short-Wave Infrared Absorption in Group-IV Nanowire Arrays

A. Attiaoui,\* É. Bouthillier, G. Daligou<sup>ID</sup>, A. Kumar, S. Assali, and O. Moutanabbir<sup>ID†</sup>

*Department of Engineering Physics, École Polytechnique de Montréal, C. P. 6079, Succ. Centre-Ville, Montréal, Québec H3C 3A7, Canada*



(Received 5 November 2020; accepted 8 December 2020; published 20 January 2021)

Engineering light absorption in the extended short-wave infrared (ESWIR) range using scalable materials is a long-sought-after capability that is crucial to implement cost-effective and high-performance sensing and imaging technologies. Herein, we demonstrate enhanced, tunable ESWIR absorption using silicon-integrated platforms consisting of ordered arrays of metastable  $\text{Ge}_{1-x}\text{Sn}_x$  nanowires with Sn content reaching 9 at.% and variable diameters. Detailed simulations are combined with experimental analyses to systematically investigate light– $\text{Ge}_{1-x}\text{Sn}_x$  nanowire interactions to tailor and optimize the nanowire-array geometrical parameters and the corresponding optical response. The diameter-dependent leaky-mode resonance peaks are theoretically predicted and experimentally confirmed with a tunable wavelength from 1.5 to  $2.2\ \mu\text{m}$ . A threefold enhancement in the absorption with respect to  $\text{Ge}_{1-x}\text{Sn}_x$  layers at  $2.1\ \mu\text{m}$  is achieved using nanowires with a diameter of 325 nm. Finite-difference time-domain simulations unravel the underlying mechanisms of the ESWIR-enhanced absorption. The coupling of the  $\text{HE}_{11}$  and  $\text{HE}_{12}$  resonant modes to nanowires is observed at diameters above 325 nm, while at smaller diameters and longer wavelengths the  $\text{HE}_{11}$  mode is guided into the underlying Ge layer. The presence of tapering in nanowires further extends the absorption range while minimizing reflection. This ability to engineer and enhance ESWIR absorption lays the groundwork to implement alternative photonic devices exploiting all-group-IV platforms.

DOI: [10.1103/PhysRevApplied.15.014034](https://doi.org/10.1103/PhysRevApplied.15.014034)

### I. INTRODUCTION

ESWIR (approximately  $1.4\text{--}2.5\ \mu\text{m}$ ) responds primarily to reflected light from objects and can penetrate fog and smog, thus enabling imaging and sensing through scattering media [1–3]. In principle, ESWIR devices can passively operate even in the dark as the nightglow from the upper atmosphere provides a natural illumination in this wavelength range. Additionally, ESWIR sensors can also be employed for thermal imaging of objects at temperatures above  $150\ ^\circ\text{C}$  [4], as well as for the spectral identification of substances sharing O—H, C—H, and N—H bonds [5,6] exploiting the strong absorbance related to molecular vibrations. Deciphering these molecular fingerprints is highly relevant for chemical and biomedical technologies. However, the high production cost and the limited spectral tunability have been a major obstacle facing the widespread adoption of ESWIR imaging and sensing capabilities [7]. Indeed, current ESWIR detectors are based predominantly on quantum-well IR photodetectors, (In,Ga)As, In-Sb, or Hg-Cd-Te [8,9]. Although most of these detectors have been explored for decades with

mature industrial platforms, limited spectral range, low responsivity, and high noise levels at room temperature have limited their use in many practical applications. As a matter of fact, these materials are prohibitively expensive, which translates into a limited imaging and sensing array size and an overall cost of a megapixel ESWIR sensor that can exceed tens of thousands of dollars [7].

An attractive alternative consists of exploiting the emerging group-IV germanium-tin ( $\text{Ge}_{1-x}\text{Sn}_x$ ) semiconductors, which exhibit a bandgap energy that can be tuned to cover the ESWIR range and beyond. Indeed, the bandgap energy in these semiconductors shrinks from, for instance,  $1.72\ \mu\text{m}$  (0.72 eV) to  $8.0\ \mu\text{m}$  (0.15 eV) as Sn content increases from 5% to 30% in the absence of any lattice strain [10–15]. However, these compositions are substantially higher than the approximately 1% solubility of Sn in Ge. To reach this compositional range, nonequilibrium growth protocols were developed to prevent phase separation and avoid Sn segregation and material degradation [12,16–21]. Interestingly,  $\text{Ge}_{1-x}\text{Sn}_x$  layers can be grown epitaxially on silicon wafers, thus allowing a full compatibility with CMOS processing needed for a full exploitation of the current microelectronic and photonic technologies. This would yield production in a high volume with repeatability, uniformity, and cost effectiveness using standard design flows.

\*anis.attiaoui@polymtl.ca

†oussama.moutanabbir@polymtl.ca

Recognizing the potential of  $\text{Ge}_{1-x}\text{Sn}_x$  as an effective building block for CMOS-compatible sensing and imaging devices, tremendous efforts have been recently expended to integrate this material system in the design and fabrication of a variety of optoelectronic and photonic devices [22–26]. This demonstrated capability of  $\text{Ge}_{1-x}\text{Sn}_x$  as a versatile, silicon-compatible ESWIR material can be further enhanced by exploiting the nanowire (NW) geometry as an additional degree of freedom to engineer and control the light-matter interaction. Indeed, NWs exhibit excellent antireflection properties over an extended wavelength range [27] and are a medium with a proven enhanced absorption and efficiency in solar cells and photodetectors [27–29]. Furthermore, NWs also provide the control over the directionality and polarization of the emitted light by simply tuning the diameter and tapering without any external optics [30–33]. The enhanced strain relaxation along the NW radial direction enabled the development of both axial and radial bottom-up  $\text{Ge}_{1-x}\text{Sn}_x$  NW heterostructures with tunable room-temperature direct band-gap emission [34–38]. Herein, we demonstrate the use of  $\text{Ge}_{1-x}\text{Sn}_x$  NW arrays on a Si wafer to achieve a tunable and enhanced ESWIR absorption. Leaky-mode resonance peaks with a variable wavelength from 1.5 to 2.2  $\mu\text{m}$  are theoretically predicted and experimentally achieved in  $\text{Ge}_{1-x}\text{Sn}_x$  NW arrays at a Sn content reaching approximately 9 at.%. The enhanced ESWIR absorption is driven by the coupling of  $\text{HE}_{11}$  mode to NWs at diameters above 325 nm, while at smaller diameters the  $\text{HE}_{11}$  mode is guided into the underlying Ge layer.

## II. METHODS

A  $\text{Ge}_{1-x}\text{Sn}_x$  layer is grown on a 4-in. Si (100) wafer in a low-pressure chemical vapor deposition (CVD) reactor using ultrapure  $\text{H}_2$  carrier gas, 10% monogermane ( $\text{GeH}_4$ ) and tin-tetrachloride ( $\text{SnCl}_4$ ) precursors [12,20,39]. First, a 1.0- $\mu\text{m}$ -thick Ge-VS is grown with a two-temperature step process at 450 and 600 °C followed by a postgrowth thermal cyclic annealing (>800 °C). Next, a 1.1- $\mu\text{m}$ -thick  $\text{Ge}_{1-x}\text{Sn}_x$  layer with a graded composition from 6.7 at.% to 9.2 at.% is grown at 320 °C for 270 min using a Ge : Sn ratio of approximately 1290 in gas phase. Afterwards, arrays with variable NW diameters and pitch length are patterned with a Raith e-line electron-beam lithography (EBL) with a beam energy of 10 kV using a negative resist (ma-N 2403). Next, a  $\text{Cl}_2$ -based reactive-ion etching (a Plasmalab 100 ICP-RIE) process is performed to etch the NWs from the  $\text{Ge}_{1-x}\text{Sn}_x$  layer. Lastly, the resist is removed using an oxygen-based plasma process (see the Supplemental Material [40]).

The UV and visible absorptance spectra of the NW arrays are collected at room temperature using a Perkin Elmer Lambda 900 Series UV/VIS/NIR Spectrometer. Spectra are acquired in the double-beam mode with

baseline correction to eliminate instrument effects. The instrument uses a 150-mm integrating sphere with an (In,Ga)As detector at a resolution of 0.5 nm (see the Supplemental Material [40]). Second, spectroscopic ellipsometry data are collected with a dual-rotating compensator and a variable angle spectroscopic ellipsometer (VASE, J.A. Woollam, Inc.) at incident angles of 62° to 84° with a 2° step from the sample normal and photon energies in the range of 0.5–1.4 eV (2.5–0.9- $\mu\text{m}$  wavelengths). The illuminated area of the sample at these angles is approximately 3×7 mm<sup>2</sup>. The experimental  $\tan(\Psi)$  and  $\cos(\Delta)$  data as well as the different optical models used are shown (see the Supplemental Material [40]).

Finally, Lumerical FDTD®, a commercial software, is used to perform three-dimensional (3D), full-field electromagnetic simulations of  $\text{Ge}_{1-x}\text{Sn}_x$  NWs. Arrays are constructed using a rectangular 3D simulation region, with periodic Bloch boundary conditions applied in the  $x$  and  $y$  directions and infinite boundary conditions, rendered as perfectly matched layers (PMLs), in the  $z$  direction. All nanowire structures are modeled as  $\text{Ge}_{1-x}\text{Sn}_x$ , using the SE-measured optical properties, and are anchored on an infinite silicon substrate with a 1- $\mu\text{m}$  Ge-VS layer. All nanowire structures are triangularly packed at a variable fill fraction, with a geometrical configuration extracted from SEM images in Figs. 2(b) and 2(c) and are 1.2  $\mu\text{m}$  in height. Furthermore, tapering is introduced in the finite-difference time-domain (FDTD) simulation to reduce any possible source of discrepancies between the simulated and the microfabricated NW arrays. A detailed description of the simulation conditions is discussed (see the Supplemental Material [40]).

## III. RESULTS AND DISCUSSION

### A. $\text{Ge}_{1-x}\text{Sn}_x$ epitaxy and NW-array fabrication

The NW arrays are dry etched from epitaxially grown 1.1- $\mu\text{m}$ -thick  $\text{Ge}_{1-x}\text{Sn}_x$  layer on a 1.0- $\mu\text{m}$ -thick Ge-on-Si virtual substrate (Ge-VS) (see Sec. II for details). The cross-section TEM and the energy dispersive x-ray spectroscopy (EDS) compositional profile are shown in Fig. 1(a). Misfit dislocations are mainly visible at  $\text{Ge}_{1-x}\text{Sn}_x$ /Ge interface as a result of the lattice-mismatched growth. The EDS profile shows a graded composition towards the surface of  $\text{Ge}_{1-x}\text{Sn}_x$  resulting from the strain relaxation during growth [20]. To evaluate both Sn content and lattice strain, x-ray-diffraction (XRD) reciprocal-space-mapping (RSM) measurements around the asymmetrical (224) reflection are carried out [Fig. 1(b)]. The small tensile strain of  $\varepsilon_{||} \sim 0.16\%$  in Ge layer is thermal mismatch-induced during cyclic annealing prior to  $\text{Ge}_{1-x}\text{Sn}_x$  growth. The incorporation of Sn across the graded  $\text{Ge}_{1-x}\text{Sn}_x$  layer increases from 6.7 to 9.2% toward the surface, while the compressive strain increases from  $\varepsilon_{||} \sim -0.2\%$  to  $\sim -0.4\%$ . The indirect nature of the  $\text{Ge}_{1-x}\text{Sn}_x$  sample is

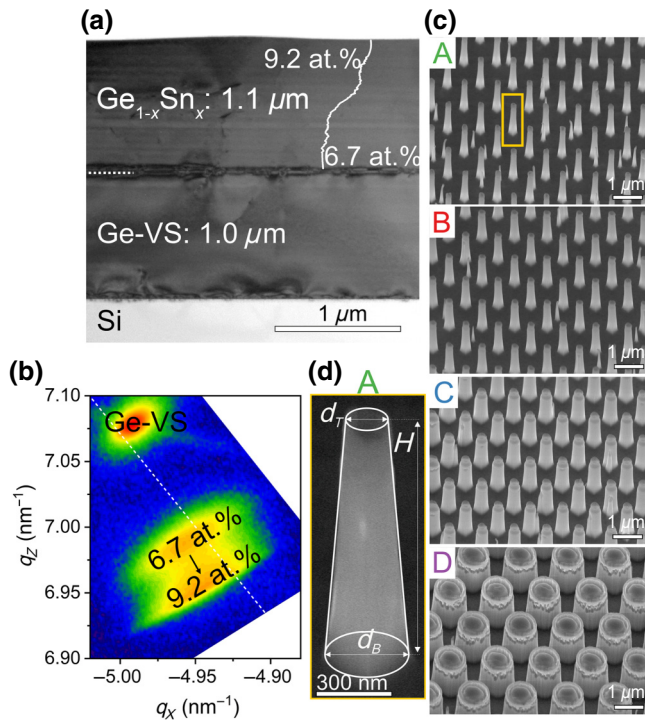


FIG. 1. (a) Cross-section TEM image of the  $\text{Ge}_{1-x}\text{Sn}_x/\text{Ge-VS}/\text{Si}$  multilayer heterostructure acquired along the [110] zone axis. The scale bar is 1  $\mu\text{m}$  (b) (224) XRD-RSM map showing the graded composition in  $\text{Ge}_{1-x}\text{Sn}_x$  from 6.7 at.% to 9.2 at.%(c) SEM micrograph of the A–D  $\text{Ge}_{1-x}\text{Sn}_x$  NW arrays (tilting angle 45°). All the scale bars are set to 1  $\mu\text{m}$  (d) Enlarged view of a single A NW from (c) with a scale bar of 300 nm.

investigated theoretically with a 30-band  $\mathbf{k} \cdot \mathbf{p}$  formalism where optical band-to-band transitions are calculated and compared along the highest symmetry directions of the Brillouin zone (mainly  $\Gamma$  and  $L$ ) (see the Supplemental Material [40]). The direct band-to-band optical transition (along the  $\Gamma$ -Brillouin zone) is redshifted from 2.05 to 2.30  $\mu\text{m}$ , when the Sn content increases from 6.7 to 9.2 at.%. Next,  $\text{Ge}_{1-x}\text{Sn}_x$  NW arrays with variable diameters are fabricated using a  $\text{Cl}_2$ -based reactive-ion etching (RIE) top-down process (see Sec. II for details) [29]. This process yields slightly tapered NWs. Tapering is expected to improve light collection and absorption, as discussed below.

Based on the systematic simulations discussed below, four different tapered NW arrays are fabricated with diameters (top and bottom) of 175 and 300 nm (A), 200 and 325 nm (B), 325 and 450 nm (C), and 375 and 550 nm (D), as shown in the SEM images in Fig. 1(c). A pitch of 1.1  $\mu\text{m}$  is used for A, B, and C NW arrays, while a pitch of 1.6  $\mu\text{m}$  is used for D NW array to account for the larger NW diameter. Few (thinner) parasitic NWs are visible in arrays A and B, while at the largest NW array diameter D the NW top surface seems to be not perfectly flat. This subtle morphological feature has no effect on the optical

TABLE I. Structural information of the different fabricated NW arrays extracted from the statistical SEM images' analysis from Fig. 1(c).

NWs	Parameters				
	$\text{Ge}_{1-x}\text{Sn}_x$ NW arrays				
	$d_T$ (nm)	$d_B$ (nm)	$u$ ( $\mu\text{m}$ )	H ( $\mu\text{m}$ )	FF (%)
A	175	300	1.1	1.2	2.1
B	200	325	1.1	1.2	2.6
C	325	450	1.1	1.2	5.6
D	375	550	1.6	1.2	3.7

response of these NWs. NW tapering, as exemplified in Fig. 1(d), originates most likely from parasitic etching of the resist on top and sidewall diffusion of ionic species during the RIE process. The height of NWs, approximately 1.3  $\mu\text{m}$ , is slightly larger than the as-grown  $\text{Ge}_{1-x}\text{Sn}_x$  layer thickness due to the partial etching of Ge layer. In addition, the compressive strain  $\varepsilon_{||} \sim -0.4\%$  in the as-grown  $\text{Ge}_{1-x}\text{Sn}_x$  layer has been fully relaxed in NWs due to the formation of free surfaces (see the Supplemental Material [40]). The geometrical parameters defining the four arrays are summarized in Table I. Before discussing the experimental measurements, the optical properties of these arrays are first evaluated based on simulations.

## B. Numerical simulations of the absorption in $\text{Ge}_{1-x}\text{Sn}_x$ NW arrays

Three-dimensional FDTD simulations are performed using the Lumerical<sup>®</sup> software package to assess the effects of the array parameters on light absorption. For precise simulations, we first develop the optical model for as-grown  $\text{Ge}_{1-x}\text{Sn}_x$  layers. In this regard, the complex dielectric function  $\hat{\epsilon} = \epsilon_1 + i\epsilon_2$  in the 0.9–2.5  $\mu\text{m}$  spectral range is estimated from spectroscopic ellipsometry (SE) measurements (see the Supplemental Material [40]). The obtained dielectric function is used as the input in FDTD simulations. The optical response of triangular arrays is investigated at a near-normal incidence (5°), equal to the experimental angle of incidence. Figure 2(a) depicts the relevant geometrical parameters used in these simulations, namely the diameter  $d$ , the pitch  $u$ , and the height  $H$ . For simplicity, cylindrical  $\text{Ge}_{0.91}\text{Sn}_{0.09}$  NWs with a uniform composition are considered in the simulations. NW tapering is also addressed as discussed below. Figure 2(b) exhibits the simulated absorptance ( $A$ ) map for a triangular array of 1.1- $\mu\text{m}$ -long  $\text{Ge}_{1-x}\text{Sn}_x$  NWs at a wavelength of 2  $\mu\text{m}$  as a function of  $d$  and  $u$  up to 1.5 and 2.2  $\mu\text{m}$ , respectively. Multiple leaky-mode resonances (LMRs) are visible at different diameters, while the pitch has a subtle effect on the absorption, as highlighted for InP NW arrays [50]. Two sharp resonances are observed at diameters of 350 and 850 nm, while the weaker dependence on the pitch is highlighted in the inset of Fig. 2(b). The extent

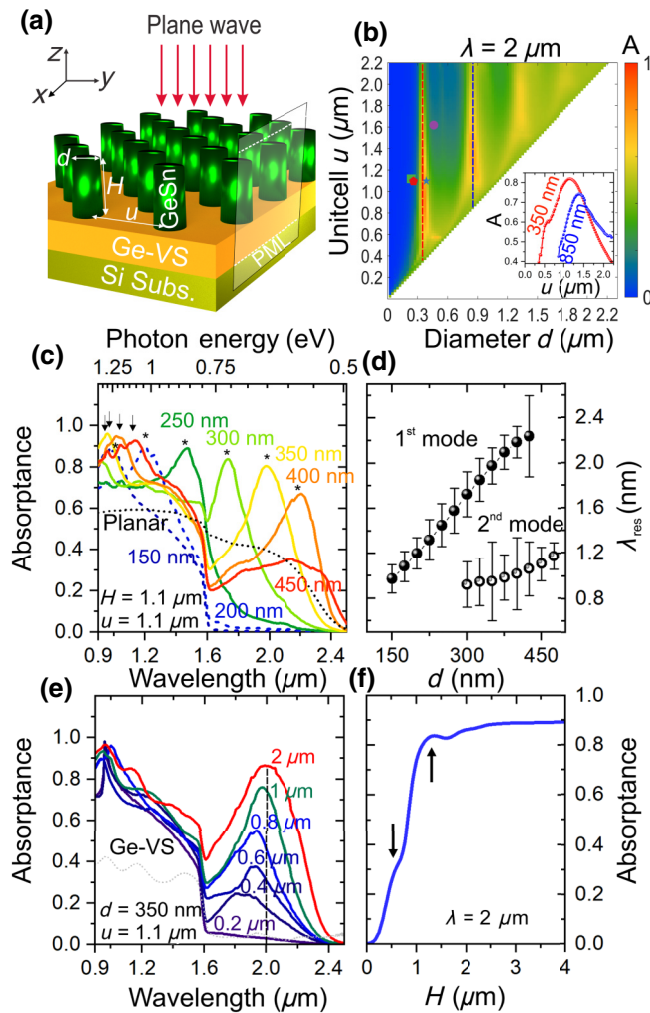


FIG. 2. (a) A 3D scheme of the cylindrical NWs in a triangular lattice. The relevant geometrical properties the height  $H$ , the diameter  $d$ , and the pitch  $u$  are indicated. The simulation domain, showing the PML region, is presented in Fig. S4(a) of the Supplemental Material [40]. The simulated absorptance of the structure presented in (a) for diameter and pitch that varies between 0 and 2.2  $\mu\text{m}$ . The inset indicates the absorptance as a function of the pitch for two fixed diameters (350 dashed-red line and 850 nm, dashed-blue line). (c) The spectral absorptance for a 1.2  $\mu\text{m}$  fixed height and a 1.1  $\mu\text{m}$  pitch and different diameters (between 150 and 450 nm). The peaks indicated by \* and ↓ are the first two excited LMR of the cylindrical NW array. The dashed-black line represents the simulated absorptance of the  $\text{Ge}_{1-x}\text{Sn}_x$  planar layer. (d) The evolution of the two LMR observed in the panel as a function the diameter of the cylindrical NW. (e) The simulated spectral absorptance for a fixed diameter of 350 nm and a fixed pitch of 1.1  $\mu\text{m}$  as a function of the height. The dashed-gray line is the simulated absorptance of only the Ge-VS layer (in other words, when  $H = 0 \mu\text{m}$ ). (f) The absorptance versus the height of the structure considered at panel (e) at a fixed wavelength of 2  $\mu\text{m}$ . The arrows indicate the Fabry-Perot resonances.

of absorption resonance decreases as  $u$  increases. The maximum absorptance  $A = 82\%$  is obtained for  $u = 1.1 \mu\text{m}$  and  $d = 350 \text{ nm}$ , whereas the increase of  $d$  up to 850 nm

shifts the absorptance peak ( $A = 74\%$ ) to a higher pitch ( $u = 1.4 \mu\text{m}$ ). It is noteworthy that the peak resonance seems insensitive to the array pitch, due to the sparse nature of NW arrays for  $d$  below 375 nm. Therefore, light coupling predominantly occurs in the localized radial resonant modes inside NWs rather than as an absorption resonance from the array periodicity. The dominant role of the waveguide modes in the absorption enhancement translates into a strong correlation between  $d$  and the incident wavelength.

The absorption spectral tunability as a function of  $d$  for a fixed pitch ( $u = 1.1 \mu\text{m}$ ) is displayed in Fig. 2(c). Multiple features are observed. First, when  $d$  increases from 150 to 400 nm the absorption peak shifts from 1.0  $\mu\text{m}$  to 2.2  $\mu\text{m}$  [indicated by \* in Fig. 2(c)]. However, a strong broadening of the peak is observed for larger  $d$ , eventually leading to a quasiplanar absorption. A detailed evolution of the corresponding mode is presented in Fig. 2(d), where the resonant wavelength scales directly with  $d$ . The resonant wavelength dependence to the NW geometry has been exhaustively studied in III-V systems, more specifically for InP [49], and  $\text{Al}_{0.10}\text{Ga}_{0.90}\text{As}$  [51]. Second, for  $d$  larger than 300 nm a second absorption peak develops in the 0.9–1.2  $\mu\text{m}$  range [indicated by ↓ in Fig. 2(c)] emerging from an extended broadband reaching Ge band gap [solid spheres in Fig. 2(d)]. Third, the maximum peak intensity progressively decreases with increasing wavelength, following almost a similar trend as the reference as-grown  $\text{Ge}_{1-x}\text{Sn}_x$  layer [black-dashed line in Fig. 2(c)]. Fourth, near Ge direct band edge (1.6  $\mu\text{m}$ ), the observed asymmetry in the absorptance peak (a sharp change between a dip and a peak) dominates the absorption enhancement at longer wavelengths (i.e., larger  $d$ ). A simplified Mie-Lorentz scattering simulation is undertaken to verify the dependence of the LMR modes to the geometrical properties of infinite-single  $\text{Ge}_{1-x}\text{Sn}_x$  NW with the same dimensions as the microfabricated ones (see the Supplemental Material [40]). Coupling among NWs and optical cross-talk[52] promotes the excitation of additional LMR when the NW density increases. The absorption peaks at approximately 90% at diameters that are multiple of  $\lambda/4 = 250 \text{ nm}$ , where the light is more efficiently coupled to NWs. For a fixed pitch of 1.1  $\mu\text{m}$ , a decrease in the maximum absorption at the resonance frequency is noticeable in Fig. 2(c) when  $d$  increases from 250 nm (approximately 90%) to 400 nm (approximately 68%). Interestingly, when  $d$  decreases below 300 nm the absorption above 1.6  $\mu\text{m}$  is rapidly suppressed. This indicates that the NW absorption cross section becomes too small to allow an effective absorption in this wavelength range. This is consistent with earlier observations in other material systems [28,53–57], and occurs when the absorption cross section is larger than the NW geometric cross section.

The effect of the NW height  $H$  on the absorptance is shown in Fig. 2(e) for  $d = 350 \text{ nm}$  and  $u = 1.1 \mu\text{m}$ . When

$H$  is lower than  $0.2 \mu\text{m}$  negligible absorption is observed and only wavelengths below  $1.6 \mu\text{m}$  are absorbed in Ge. For comparison, the measured absorptance of the as-grown  $1\text{-}\mu\text{m}$ -thick Ge layer is also shown in Fig. 2(e). By increasing  $H$  from  $0.4$  to  $2 \mu\text{m}$ , an absorption peak develops with a gradual increase in intensity up to approximately 86%, while the resonant wavelength ( $\lambda_{\text{res}}$ ) shifts from  $1.7$  to  $2.0 \mu\text{m}$  [Fig. 2(e)]. This effect is related to the presence of Fabry-Perot (FP) modes in the vertical NW cavity. The latter can be highlighted by plotting the absorptance as a function of  $H$  [Fig. 2(f)], where local maxima (indicated by black arrows) are separated by approximately  $0.8 \mu\text{m}$ . Resonant modes are allowed when  $H$  is a multiple of  $m\lambda/2n$ , where  $m$  is an integer and  $n$  is the effective refractive index. Considering  $n=4.1$  for  $\text{Ge}_{1-x}\text{Sn}_x$ , at a wavelength of  $2.0 \mu\text{m}$  the FP spacing is approximately  $0.24 \mu\text{m}$ , in agreement with the local maxima of  $0.56$  ( $m=2$ ) and  $1.3 \mu\text{m}$  ( $m=5$ ) indicated in Fig. 2(f). Therefore, the proposed NW-array design results in a sizable enhancement in the  $\text{Ge}_{1-x}\text{Sn}_x$  absorption at  $2.0 \mu\text{m}$  wavelength when  $H$  exceeds  $0.7 \mu\text{m}$ .

### C. Optical properties of $\text{Ge}_{1-x}\text{Sn}_x$ NW arrays

The simulations outlined above are used to guide the fabrication of  $\text{Ge}_{1-x}\text{Sn}_x$  NW arrays and investigate their optical response in the ESWIR range. As highlighted earlier in Fig. 1, the NWs are tapered and thus the FDTD simulations should also include this morphological feature to allow a more accurate correlation with the experimental observations. Tapering induces a broadening of the LMR peaks (see the Supplemental Material [40]) while it is expected to minimize the reflectivity [58] and increase light absorption [59]. Additionally, tapering increases the NW fill factor (FF) from approximately 2% at the top to 5% at the bottom in average for all arrays (see the Supplemental Material [40]). The FF below 5% suggests that the arrays in our geometrical model are sparse, resulting in very minimal coupling between NWs [60]. Therefore, from the near-field simulations, we conclude that short wavelengths are absorbed in the top part of  $\text{Ge}_{1-x}\text{Sn}_x$  NWs, while at longer wavelengths the tapering contributes the strongest to the absorption. The straight cylindrical NW arrays show a well-defined, diameter-dependent absorption resonance, whereas tapered NW arrays show a broad absorption over the entire wavelength range. This behavior agrees well with earlier observations for Si NWs [61]. Tapered NWs consist of a continuous range of diameters along the NW axis; hence, it is possible to absorb almost the entire wavelength range in the ESWIR. Notably, tapering introduces mode broadening, which translates to a broader resonance peak in absorptance, when compared to cylindrical NW. However, the magnitude of the absorptance is minimally affected. Data points representing the four fabricated arrays are overlaid (green square for A,

red pentagon for B, blue star for C, and purple circle for D) in the absorption map in Fig. 2(b) to highlight the expected absorption. Measurements on these NW arrays are performed at room temperature in an integrating sphere optical setup (see Sec. II for more details).

The experimental absorptance spectra recorded for the four arrays are plotted in Figs. 3(a) and 3(d) together with the simulated FDTD absorptance spectra (dashed black line). In planar  $\text{Ge}_{1-x}\text{Sn}_x$ , the absorptance gradually decreases from 40% at  $0.9 \mu\text{m}$  to less than 5% at  $2.4 \mu\text{m}$  [gray curve in Fig. 3(a)]. The oscillations between  $1.6$  and  $2.1 \mu\text{m}$  result from FP resonance between Ge and  $\text{Ge}_{1-x}\text{Sn}_x$  layers. In NW arrays with smaller diameters (A and B), the absorption is enhanced by a factor of approximately 2 compared to planar geometry for wavelengths shorter than  $1.6 \mu\text{m}$ , i.e., below the Ge band gap. However, a monotonic decrease in the absorption is visible at longer wavelengths [Figs. 3(a) and 3(b)]. For the arrays with larger diameters (C and D), an additional absorption peak develops above  $1.6 \mu\text{m}$  with a maximum intensity at approximately  $2.0 \mu\text{m}$ , which is more than 1.6 times higher than in planar  $\text{Ge}_{1-x}\text{Sn}_x$  [Figs. 3(c) and 3(d)]. Regardless of the diameter, the measured absorptance is in very good quantitative agreement with FDTD simulations (dashed lines), thus confirming that NW arrays strongly enhance the absorption.

We note that the small offset in arrays C and D peak positions can be explained by light scattering due to the presence of parasitic NWs, Ge layer overetching, and the fluctuations in diameter and tapering (see the Supplemental Material [40]). In a sparse NW array (with an FF below 5%), radial LMR are the primary mechanism responsible for resonant absorption [62,63]. Harnessing these resonant modes in  $\text{Ge}_{1-x}\text{Sn}_x$  materials can in principle permit the absorption enhancement in the ESWIR spectral range. Accordingly, to validate that radial LMR is the responsible mechanism for light-absorption enhancement, modal numerical simulations are performed to decouple the strongly wavelength-dependent effects of optical energy propagation along NWs, diffraction by the periodic array (i.e., photonic crystal effects), and FP-type resonances (reflections at top and bottom sections of the NWs). To achieve high absorption in NWs, the modes must couple to incident plane waves, strongly resonate between the top (air) and bottom (Ge) interfaces, and their absorbed energy needs to be confined within the NW. The resonance modes, indicated by arrows in Figs. 3(a) and 3(d), are calculated for each structure. The peak position of the resonance modes is extracted from the electric field intensity as a function of wavelength in all the NW arrays, as shown in the gray shaded region in Figs. 3(a) and 3(d). The mismatch between the measured and calculated LMR position is associated to the microfabrication imperfection (mainly tapering) and the Ge-layer underetching (see the Supplemental Material [40]). Typically, these

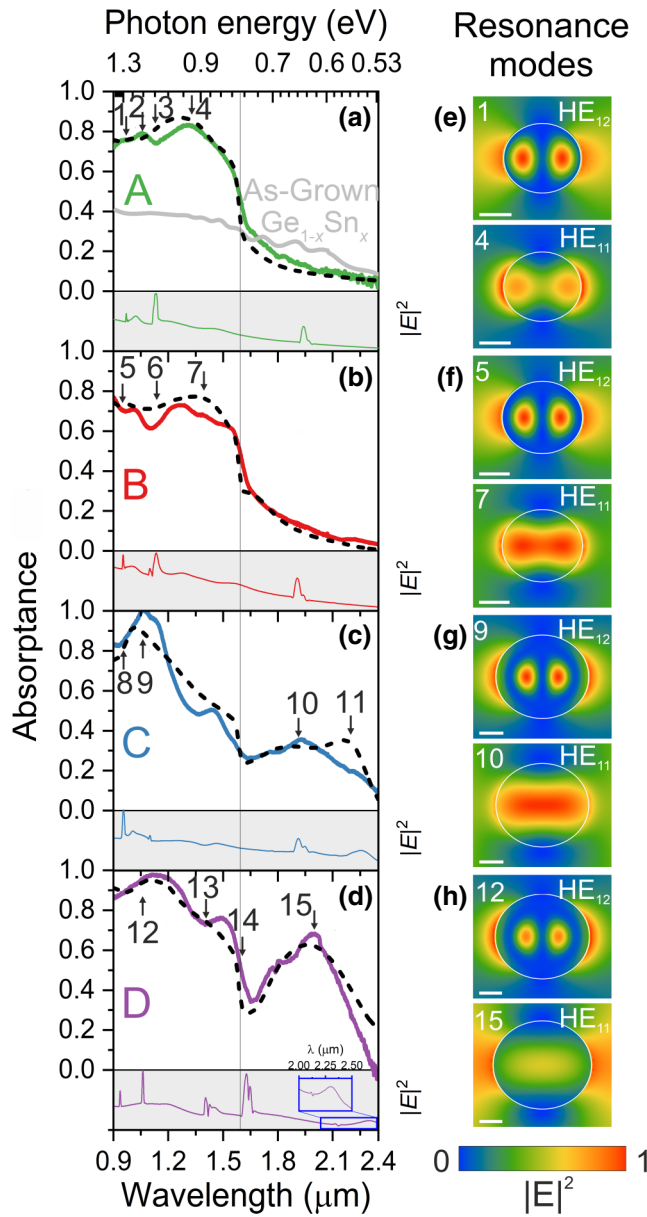


FIG. 3. (a)–(d) The spectral absorptance of the four NW arrays structures (A–D) measured with the integrating sphere between 0.9 and 2.4  $\mu\text{m}$ . The corresponding dashed lines are the simulated FDTD response of the NW arrays, calculated based upon the structure shown in Fig. 2(a). The numbered arrows correspond to the HE<sub>11</sub> and HE<sub>12</sub> resonance modes observed for each structure, as extracted from the electric field intensity as a function of wavelength shown in the gray shaded region for each NW array. (e), (f) The corresponding normalized electric field  $|E|^2$  distribution for each corresponding resonance peak of the HE<sub>11</sub> and HE<sub>12</sub> modes. The panel numbers are correlated to the resonance peak position in (a)–(d) and are presented in Table II. The scale bar for all the electric field maps is set to 100 nm.

departures from perfect fidelity result in peak broadening and reduced absorption, which accounts for the main discrepancy between the experiments and simulations.

TABLE II. Fundamental HE<sub>11</sub> and HE<sub>12</sub> excited mode resonances for all the Ge<sub>1-x</sub>Sn<sub>x</sub> NW nanostructures (A–D).

Array	Modes	Parameters				
		Ge <sub>1-x</sub> Sn <sub>x</sub> NW arrays				
		Peak no.	$\lambda_0$ (nm)	$n_\alpha$	$q_{\text{rad}}$	$Q$
A	HE <sub>12</sub>	1	970	1.15-i1.66	1.445	143
	HE <sub>11</sub>	2	1040	3.35-i0.33	0.099	NA
	HE <sub>11</sub>	3	1128	3.03-i0.32	0.107	45
	HE <sub>11</sub>	4	1305	2.33-i0.33	0.142	NA
B	HE <sub>12</sub>	5	950	2.03-i0.69	0.340	88
	HE <sub>11</sub>	6	1130	3.32-i0.30	0.090	40
	HE <sub>11</sub>	7	1250	2.95-i0.29	0.100	NA
C	HE <sub>12</sub>	8	1005	3.12-i0.35	0.112	20
	HE <sub>12</sub>	9	1085	4.02-i0.27	0.067	NA
	HE <sub>11</sub>	10	1946	2.63-i0.22	0.084	50
	HE <sub>11</sub>	11	2202	2.11-i0.16	0.076	10
D	HE <sub>12</sub>	12	1060	3.64-i0.30	0.083	65
	HE <sub>11</sub>	13	1405	3.80-i0.21	0.055	74
	HE <sub>11</sub>	14	1627	3.56-i0.20	0.056	113
	HE <sub>11</sub>	15	2003	3.14-i0.19	0.062	NA

NA: not available.

#### D. Modal analysis of Ge<sub>1-x</sub>Sn<sub>x</sub> NW arrays

The resonance modes have low-quality factor ( $Q$ ) in the range of 30–150. The quality factor  $Q$  for each one of the fabricated NW arrays is presented in Table II and the Supplemental Material [40]. Adjacent peaks are observed, for all the arrays, between 0.9–1.3  $\mu\text{m}$  and give rise to enhanced broadband absorption through strong in coupling between incident light and the modes due to their low  $Q$ . Light with low- $Q$  wavelengths has been shown to easily couple into the mode [64–66]. Above 1.3  $\mu\text{m}$ , the number of resonance modes increases when the NW diameter increases. For instance, arrays A and B present only one clear peak (with an average  $Q$  of 85), located at 1.9  $\mu\text{m}$  as well as some small oscillations induced by FP resonances. The same behavior holds true for array C apart from the appearance of an additional resonance at 2.2  $\mu\text{m}$  with a low- $Q$  factor of 20. Finally, array D is marked with the presence of two well-defined modes at 1.4 and 1.6  $\mu\text{m}$ , with an average  $Q$  of 140. This suggests that higher- $Q$ , subwavelength resonators may be achievable for larger diameter structures through the introduction of higher-order modes, while gaining spectral bandwidth through a lower- $Q$  fundamental mode, which is shifted to longer wavelengths.

A close examination of the corresponding  $x$ - $y$  cross-section distribution of the electric field ( $|E|^2$ ) and the magnetic field ( $|H_z|^2$ , see the Supplemental Material [40]) for the resonance mode at specific resonance wavelength [indicated by arrows in Figs. 3(a) and 3(d)], taken at a height of 45% of the NW height, provides further insights

into the LMR absorption behavior and reveals useful features [Figs. 3(e) and 3(h)]. First, different types of resonant modes are excited in NW cavities: leaky resonance and lower-order two-dimensional resonant modes. Second, different types of mode profiles emerge as the NW diameter increases. In the smallest diameter NW array A, the HE<sub>12</sub> one-dimensional leaky higher-order mode with two nodes appears [Fig. 3(e)] at shorter wavelengths (peak 1), whereas above 1  $\mu\text{m}$  (peaks 2, 3, and 4) the fundamental HE<sub>11</sub> mode is excited. The latter shows large modal delocalization to the NW surrounding and has no cut-off frequency. A significant spillover into the surrounding air is evident [panel 4 in Fig. 3(e)]. A slight increase in the NW diameter (B) does not have any significant impact on the electric field profile, except a broadening of the HE<sub>11</sub> mode [panel 7 of Fig. 3(f)]. Note that in NW arrays A and B, the absorbed incident energy is localized fully inside the NW below 1.6  $\mu\text{m}$  (peaks 1–4) for A and B (peaks 5–7) [Figs. 3(a) and 3(b)]. Furthermore, only the HE<sub>11</sub> mode is guided into Ge underneath the NW and strongly enhances the absorption above the Ge band gap, as the cut-off wavelength of the HE<sub>12</sub> mode is below 1  $\mu\text{m}$  for A and B arrays. For the NW array C with larger diameter (325/450 nm), the HE<sub>12</sub> mode appears to be more spatially confined inside the NW below 1.61  $\mu\text{m}$  [panel 9 in Fig. 3(g)], and it starts to broaden to cover a larger coupling area inside the NW above 1.61  $\mu\text{m}$  [panel 10 in Fig. 3(g)] until finally the HE<sub>11</sub> mode is excited at higher wavelength [peak 11 in Fig. 3(c)]. With a further increase in the NW diameter and pitch in array D, higher coupling efficiency for the HE<sub>11</sub> mode of 68% is reached at 2.0  $\mu\text{m}$  (peak 15). Enhanced absorption at MIR wavelengths is measured in randomly distributed undoped III-V NWs [(In,As)Sb], thus highlighting the usefulness of controlling LMR [67].

For a more detailed understanding of the distinct resonance behaviors of the Ge<sub>1-x</sub>Sn<sub>x</sub> NW arrays, the distribution of the Poynting vector ( $|S|^2$ ) in the  $z$ - $x$  plane is simulated at specific resonance wavelengths (0.97  $\mu\text{m}$  for A, 1.93  $\mu\text{m}$  for B, 1.76  $\mu\text{m}$  for C and 2.10  $\mu\text{m}$  for D), as shown in Fig. 4(a). Incident light is guided to the Ge layer in B at a wavelength of 1.93  $\mu\text{m}$  above the Ge band edge. For array A, the guided wave attenuates rapidly and does not reach the bottom and is localized in the top of the NWs. For arrays C and D, the incident energy is concentrated inside the NW above 1.6  $\mu\text{m}$ , which is due to an increase in the absorption cross section, enhanced by the resonant modes. Next, by analyzing the calculated  $|E_x|^2$  and  $|E_z|^2$  distributions in the  $x$ - $y$  plane at different NW heights (0.1, 0.45, and 0.9  $\mu\text{m}$ ), the leaky resonance nature of the modes can be better quantified [Fig. 4(b)]. The calculated  $|E_x|^2$  distribution in the  $x$ - $y$  plane confirms much stronger leaky-mode (HE<sub>11</sub>) resonances in the top part of the NW array D (eightfold increase in the electric field intensity). Likewise, the  $|E_z|^2$  distribution also shows a strong and broadened leaky-mode (HE<sub>12</sub>) resonance, at

the NW top, as shown in Fig. 4(b). Interestingly, different mode symmetries are degenerated even at single resonance frequency, showing the EH<sub>22</sub>, TM<sub>03</sub>, and HE<sub>13</sub> modes at the wavelength of 0.94  $\mu\text{m}$  for D NW, while at a higher wavelength of 2.10  $\mu\text{m}$ , the D NW shows TM<sub>21</sub>, TM<sub>01</sub>, and TM<sub>11</sub> mode symmetries [Fig. S11(a), see the Supplemental Material [40]]. This suggests that the stronger and broader absorption peaks [12 and 15 in Fig. 3(d) for the D NW array] observed in the spectrum might originate from these substantial transverse components of the magnetic field, giving rise to enhanced coupling with the higher-order mode resonances. The HE<sub>11</sub> mode is concentrated inside and around the NW and thus should not be affected by the order or position of the vertical NW, as long as the nanowires are not too close together. When the NWs are close, the modes couple together and the absorption peaks begin to broaden.

Yee's mesh-based full-vectorial finite-difference mode solver is used within Lumerical® in order to evaluate the modal effective index ( $n_\alpha$ :  $\alpha$  is the number of the mode) for all the investigated arrays. In all samples,  $n_\alpha$  is a complex number where the real part increases and the imaginary part decreases as the mode number increases

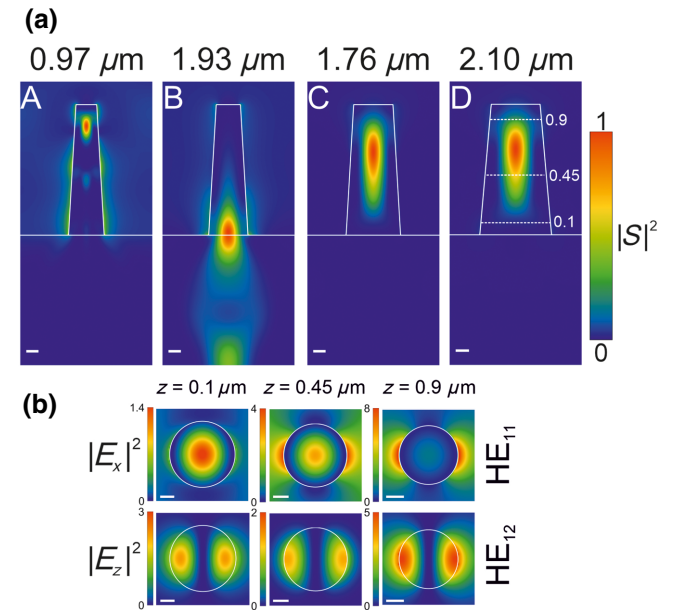


FIG. 4. (a) Calculated Poynting vector distribution in the  $z$ - $x$  plane at resonance wavelengths of 0.97, 1.93, 1.76, and 2.10  $\mu\text{m}$  for the tapered NW array structures A–D, respectively. The color scale for background profile indicates the relative magnitude of Poynting vector, normalized by the maximum magnitude. The scale bar is equal to 100 nm. (b) Calculated  $|E_x|^2$  and  $|E_z|^2$  distribution in the  $x$ - $y$  plane of the D NW array at different  $z$  position, indicated in (a) D by the horizontal dashed lines. Three different heights  $z$  (0.1, 0.45, and 0.9  $\mu\text{m}$ ) are analyzed. The  $|E_x|^2$  field patterns correspond to HE<sub>11</sub> mode, whereas the  $|E_z|^2$  correspond to HE<sub>12</sub> mode. The scale bar is 100 nm.

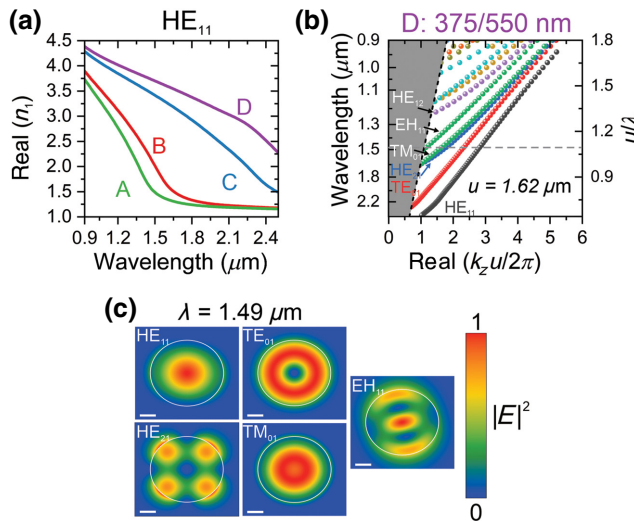


FIG. 5. (a) Dispersion of the optical fundamental mode  $\text{HE}_{11}$  in all the NW arrays (A–D). (b) Dispersion relation for the eigenmodes of the D NW array with a diameter of 375/550 nm. (c) the corresponding optical modes excited by the D NW array at a wavelength of  $1.49 \mu\text{m}$  [the gray line in (b)]. The scale bar is 100 nm.

[see the Supplemental Material [40], Fig. S11(b)], thus indicating that these evanescent modes decay exponentially into the NW array. Besides, higher-order modes occur at higher frequencies (i.e., shorter wavelengths) and have a reduced radiative loss ( $q_{\text{rad}}$ ), or put differently they are harder to couple to from free space, which implies smaller total absorption and narrower spectral width [68]. The radiative loss of the fundamental mode is defined and displayed within the Supplemental Material [40]. The match of the radiative loss of arrays C and D and the absorption loss create a critical coupling [69] between the incident radiation and  $\text{Ge}_{1-x}\text{Sn}_x$  material due to time-reversal symmetry, which explains the ESWIR resonance in these arrays. Table II shows the different resonant wavelengths for both leaky modes  $\text{HE}_{11}$  and  $\text{HE}_{12}$ , where the corresponding complex modal effective index  $n_\alpha$  as well as the radiative loss  $q_{\text{rad}}$  are presented. The increase in the radiative loss for the  $\text{HE}_{11}$  mode above  $1.6 \mu\text{m}$  for arrays C and D is a clear indication of the enhanced incident light coupling to NWs at SWIR wavelengths. For comparison, above  $1.6 \mu\text{m}$ ,  $q_{\text{rad}}$  is below 0.03 for arrays A and B. This giant increase in absorptance coincides well with the enhancement observed in the radiative loss as discussed earlier.

To further investigate the fundamental mode evolution as a function of the wavelength, we now consider the photonic crystal effect originating from the ordered NW array configuration. Note that there is a close relation between the optical eigenmodes we solve for and the modes solved for in the case of a photonic crystal band structure: the modes we solve for at normal incidence correspond to

the modes at the  $\Gamma$  point of the photonic crystal. However, since a scattering problem is considered, we must also solve for the evanescent modes at a given wavelength, whereas for the photonic crystal band structure, only the propagating modes with a real-valued propagating constant  $k_z$  are solved for. The dispersion relation for the fundamental  $\text{HE}_{11}$  mode in each array is presented in Fig. 5(a). As the wavelength increases, each array mode converges to one specific  $\text{HE}_{11}$  mode. Note that when the wavelength is smaller than the cut-off between a multi-mode and a single-mode regime ( $1.3 \mu\text{m}$  for A,  $1.4 \mu\text{m}$  for B,  $1.5 \mu\text{m}$  for C, and  $1.8 \mu\text{m}$  for D), the mode is expected to show considerable coupling between neighboring NWs. To couple to an incident plane wave at normal incidence, a Bloch mode must have an even in-plane field distribution. The electric field distribution for NW array D in Fig. 4(b) illustrates that the fundamental mode can be coupled to the incident field to yield high absorption at the resonant wavelengths. Interestingly, the extraordinary high mode coupling obtained in NW arrays C and D [see the Supplemental Material [40], Fig. S11(b)] explains well the strong absorption enhancement measured above  $1.6 \mu\text{m}$  [Figs. 3(c) and 3(d)]. The real part of the dispersion relation for the unpolarized modes in the D sample is shown in Fig. 5(b), overlaid with the light line (black-dashed line) that delimits the boundary with the region where the leaky modes' transition to guided modes occurs. Near  $2 \mu\text{m}$  [peak 15 in Fig. 3(d)], only two modes ( $\text{HE}_{11}$  and  $\text{TE}_{01}$ ) contribute to light absorption inside the NW array D. The fundamental  $\text{HE}_{11}$  mode is fairly flat for high values of  $k_z$ , but becomes slightly perturbed as it approaches the light line. This effect is clearer for  $\text{HE}_{21}$  and  $\text{TM}_{01}$  modes where the distortion of the parallel wavevector  $k_z$  is more pronounced closest to the light line. The nature of each leaky waveguide mode is determined from the normalized electric field distribution at  $1.49 \mu\text{m}$  [gray line in Fig. 5(b)], shown in Fig. 5(c), where three additional leaky modes ( $\text{HE}_{21}$ ,  $\text{TM}_{01}$ , and  $\text{EH}_{11}$ ) contribute to the light absorption shown at peak 13 in Fig. 3(d).

#### IV. CONCLUSION

Light absorption in  $\text{Ge}_{1-x}\text{Sn}_x$  NW arrays on Si is investigated by combining theoretical and experimental analyses. These systematic studies confirmed the ability to engineer and enhance light absorption in the ESWIR range using  $\text{Ge}_{0.91}\text{Sn}_{0.09}$  NW arrays. LMR-induced field enhancements in NWs yield an absorption of approximately 70% at  $2 \mu\text{m}$ , which translates into a threefold increase relative to as-grown  $\text{Ge}_{1-x}\text{Sn}_x$  layers. The NW tapering extends the absorption range and enables a broadband absorption with minimized reflection. The spectral tunability of the LMR showed geometry-dependent, specific absorption resonances in agreement with the FDTD simulations. The latter unraveled that the  $\text{HE}_{11}$  and  $\text{HE}_{12}$

optical modes are excited for all NWs. Further investigations of the spectral evolution of the modes revealed that modal broadening is the main physical mechanism linked to the absorption enhancement within NWs with larger diameters. The ability to tailor ESWIR absorption using an all-group-IV semiconductor platform lays the groundwork to harness a range of the electromagnetic spectrum that has been heretofore mainly accessible using compound III-V semiconductors. These capabilities enabled by  $\text{Ge}_{1-x}\text{Sn}_x$  NW arrays would create valuable opportunities to engineer Si-integrated, scalable photonic, and optoelectronic devices operating in the ESWIR range that benefit from the very low losses and high optical mode confinement of Si waveguides. Future works will focus on harnessing these enhanced optical response to implement and test nanowire array devices for applications including data communication, [70] biomedical sensing, and imaging.

## ACKNOWLEDGMENTS

The authors thank J. Bouchard for the technical support with the CVD system, M. Attala for fruitful discussions, B. Baloukas for support with the integrating sphere measurement. O.M. acknowledges support from NSERC Canada (Discovery, SPG, and CRD Grants), Canada Research Chairs, Canada Foundation for Innovation, Mitacs, PRIMA Québec, and Defence Canada (Innovation for Defence Excellence and Security, IDEaS). S.A. acknowledges support from Fonds de recherche du Québec-Nature et technologies (FRQNT, PBEEE scholarship).

The authors declare no competing financial interest.

- [1] M. P. Hansen and D. S. Malchow, in *SPIE*, edited by V. P. Vavilov, D. D. Burleigh, 2008), Vol. 6939, pp. 69390I.
- [2] R. G. Driggers, V. Hodgkin, and R. Vollmerhausen, in *Infrared Imaging Systems: Design, Analysis, Modeling, and Testing XXIV*, edited by G. C. Holst, K. A. Krapels, 2013), Vol. 8706, pp. 87060L.
- [3] J. Green and T. Robinson, in *Infrared Imaging Systems: Design, Analysis, Modeling, and Testing XXV*, edited by G. C. Holst, K. A. Krapels, G. H. Ballard, J. A. Buford, R. L. Murrer, 2014), Vol. 9071, pp. 90710U.
- [4] M. Wen, L. Wei, X. Zhuang, D. He, S. Wang, and Y. Wang, High-sensitivity short-wave infrared technology for thermal imaging, *Infrared Phys. Technol.* **95**, 93 (2018).
- [5] J. M. Schmitt, Optical coherence tomography (OCT): A review, *IEEE J. Sel. Top. Quantum Electron.* **5**, 1205 (1999).
- [6] M. U. Pralle, J. E. Carey, H. Homayoon, J. Sickler, X. Li, J. Jiang, F. Sahebi, C. Palsule, and J. McKee, in *Proc. SPIE*, edited by G. C. Gilbreath, C. T. Hawley, 2013), Vol. 8734, pp. 87340H.
- [7] Y. Yang, Y. H. Zhang, W. Z. Shen, and H. C. Liu, Semiconductor infrared up-conversion devices, *Prog. Quantum Electron.* **35**, 77 (2011).
- [8] N. K. Dhar, R. Dat, and A. K. Sood, in *Optoelectronics - Advanced Materials and Devices*, edited by S. Pyshkin, J. Ballato (InTech, 2013).
- [9] A. Rogalski, Infrared detectors: An overview, *Infrared Phys. Technol.* **43**, 187 (2002).
- [10] A. Attiaoui and O. Moutanabbir, Indirect-to-direct band gap transition in relaxed and strained  $\text{Ge}_{1-x-y}\text{Si}_x\text{Sn}_y$  ternary alloys, *J. Appl. Phys.* **116**, 063712 (2014).
- [11] N. Von Den Driesch, D. Stange, S. Wirths, G. Mussler, B. Holländer, Z. Ikonic, J. M. Hartmann, T. Stoica, S. Mantl, D. Grützmacher, and D. Buca, Direct bandgap group IV epitaxy on Si for laser applications, *Chem. Mater.* **27**, 4693 (2015).
- [12] S. Assali, J. Nicolas, S. Mukherjee, A. Dijkstra, and O. Moutanabbir, Atomically uniform Sn-rich GeSn semiconductors with 3.0–3.5  $\mu\text{m}$  room-temperature optical emission, *Appl. Phys. Lett.* **112**, 251903 (2018).
- [13] S. Assali, A. Dijkstra, A. Attiaoui, É. Bouthillier, J. E. M. Havercort, and O. Moutanabbir, Mid-infrared emission and absorption in strained and relaxed GeSn semiconductors, *Phys. Rev. Applied* (in press). <https://journals.aps.org/prapplied/accepted/6b076A23E861cc0a727210b94224e6c5874c8602>.
- [14] H. Tran, W. Du, S. A. Ghetmiri, A. Mosleh, G. Sun, R. A. Soref, J. Margetis, J. Tolle, B. Li, H. A. Naseem, and S. Q. Yu, Systematic study of  $\text{Ge}_{1-x}\text{Sn}_x$  absorption coefficient and refractive index for the device applications of Si-based optoelectronics, *J. Appl. Phys.* **119**, 0 (2016).
- [15] C. Xu, P. M. Wallace, D. A. Ringwala, S. L. Y. Chang, C. D. Poweleit, J. Kouvettakis, and J. Menéndez, Mid-infrared (3–8  $\mu\text{m}$ )  $\text{Ge}_{1-y}\text{Sn}_y$  alloys ( $0.15 < y < 0.30$ ): Synthesis, structural, and optical properties, *Appl. Phys. Lett.* **114**, 212 104 (2019).
- [16] S. Wirths, R. Geiger, N. V. Den Driesch, G. Mussler, T. Stoica, S. Mantl, Z. Ikonic, M. Luysberg, S. Chiussi, J. M. Hartmann, H. Sigg, J. Faist, D. Buca, and D. Grützmacher, Lasing in direct-bandgap GeSn alloy grown on Si, *Nat. Photonics* **9**, 88 (2015).
- [17] J. Margetis, S. Al-Kabi, W. Du, W. Dou, Y. Zhou, T. Pham, P. Grant, S. Ghetmiri, A. Mosleh, B. Li, J. Liu, G. Sun, R. Soref, J. Tolle, M. Mortazavi, and S.-Q. Yu, Si-Based GeSn lasers with wavelength coverage of 2–3  $\mu\text{m}$  and operating temperatures up to 180 K, *ACS Photonics* **5**, 827 (2018).
- [18] V. Reboud, A. Gassend, N. Pauc, J. Aubin, L. Milord, Q. M. Thai, M. Bertrand, K. Guillo, D. Rouchon, J. Rothman, T. Zabel, F. Armand Pilon, H. Sigg, A. Chelnokov, J. M. Hartmann, and V. Calvo, Optically pumped GeSn microdisks with 16% Sn lasing at 3.1  $\mu\text{m}$  up to 180 K, *Appl. Phys. Lett.* **111**, 092101 (2017).
- [19] A. Attiaoui, S. Wirth, A.-P. Blanchard-Dionne, M. Meunier, J. M. Hartmann, D. Buca, and O. Moutanabbir, Extreme IR absorption in group IV-SiGeSn core-shell nanowires, *J. Appl. Phys.* **123**, 223102 (2018).
- [20] S. Assali, J. Nicolas, and O. Moutanabbir, Enhanced Sn incorporation in GeSn epitaxial semiconductors via strain relaxation, *J. Appl. Phys.* **125**, 025304 (2019).
- [21] J. Margetis, S.-Q. Yu, N. Bhargava, B. Li, W. Du, and J. Tolle, Strain engineering in epitaxial  $\text{Ge}_{1-x}\text{Sn}_x$ : A path

- towards low-defect and high Sn-content layers, *Semicond. Sci. Technol.* **32**, 124006 (2017).
- [22] D. Stange, S. Wirths, R. Geiger, C. Schulte-Braucks, B. Marzban, N. V. Den Driesch, G. Mussler, T. Zabel, T. Stoica, J. M. Hartmann, S. Mantl, Z. Ikonic, D. Grützmacher, H. Sigg, J. Witzens, and D. Buca, Optically pumped GeSn microdisk lasers on Si, *ACS Photonics* **3**, 1279 (2016).
- [23] D. Stange, N. von den Driesch, T. Zabel, F. Armand-Pilon, D. Rainko, B. Marzban, P. Zaumseil, J. Hartmann, Z. Ikonic, G. Capellini, S. Mantl, H. Sigg, J. Witzens, D. Grützmacher, and D. Buca, Gesn/SiGeSn heterostructure and multi quantum well lasers, *ACS Photonics* **5**, 4628 (2018).
- [24] Y. Zhou, W. Dou, W. Du, S. Ojo, H. Tran, S. A. Ghetmiri, J. Liu, G. Sun, R. Soref, J. Margetis, J. Tolle, B. Li, Z. Chen, M. Mortazavi, and S.-Q. Yu, Optically pumped GeSn lasers operating at 270 K with broad waveguide structures on Si, *ACS Photonics* **6**, 1434 (2019).
- [25] J. Chrétien, N. Pauc, F. Armand Pilon, M. Bertrand, Q.-M. Thai, L. Casiez, N. Bernier, H. Dansas, P. Gergaud, E. Delamadeleine, R. Khazaka, H. Sigg, J. Faist, A. Chelnokov, V. Reboud, J.-M. Hartmann, and V. Calvo, Gesn lasers covering a wide wavelength range thanks to uniaxial tensile strain, *ACS Photonics* **6**, 2462 (2019).
- [26] H. Tran, T. Pham, J. Margetis, Y. Zhou, W. Dou, P. C. Grant, J. M. Grant, S. Al-Kabi, G. Sun, R. A. Soref, J. Tolle, Y.-H. Zhang, W. Du, B. Li, M. Mortazavi, and S.-Q. Yu, Si-Based GeSn photodetectors toward Mid-infrared imaging applications, *ACS Photonics* **6**, 2807 (2019).
- [27] S. L. Diedenhofen, O. T. A. Janssen, G. Grzela, E. P. A. M. Bakkers, and J. Gómez Rivas, Strong geometrical dependence of the absorption of light in arrays of semiconductor nanowires, *ACS Nano* **5**, 2316 (2011).
- [28] P. Krogstrup, H. I. Jørgensen, M. Heiss, O. Demichel, J. V. Holm, M. Aagesen, J. Nygård, and A. Fontcuberta i Morral, Single-nanowire solar cells beyond the shockley-queisser limit, *Nat. Photonics* **7**, 306 (2013).
- [29] D. Van Dam, N. J. J. Van Hoof, Y. Cui, P. J. Van Veldhoven, E. P. A. M. Bakkers, J. Gómez Rivas, and J. E. M. Haverkort, High-Efficiency nanowire solar cells with omnidirectionally enhanced absorption Due to self-aligned indium-Tin-oxide Mie scatterers, *ACS Nano* **10**, 11414 (2016).
- [30] D. Van Dam, D. R. Abujetas, R. Paniagua-Domínguez, J. A. Sánchez-Gil, E. P. A. M. Bakkers, J. E. M. Haverkort, and J. Gómez Rivas, Directional and polarized emission from nanowire arrays, *Nano Lett.* **15**, 4557 (2015).
- [31] G. Grzela, R. Paniagua-Domínguez, T. Barten, Y. Fontana, J. A. Sánchez-Gil, and J. G. Rivas, Nanowire antenna emission, *Nano Lett.* **12**, 5481 (2012).
- [32] M. E. Reimer, G. Bulgari, N. Akopian, M. Hocevar, M. B. Bavinck, M. A. Verheijen, E. P. A. M. Bakkers, L. P. Kouwenhoven, and V. Zwiller, Bright single-photon sources in bottom-up tailored nanowires, *Nat. Commun.* **3**, 737 (2012).
- [33] G. Bulgari, M. E. Reimer, M. Bouwes Bavinck, K. D. Jöns, D. Dalacu, P. J. Poole, E. P. A. M. Bakkers, and V. Zwiller, Nanowire waveguides launching single photons in a Gaussian mode for ideal fiber coupling, *Nano Lett.* **14**, 4102 (2014).
- [34] S. Biswas, J. Doherty, D. Saladukha, Q. Ramasse, D. Majumdar, M. Upmanyu, A. Singha, T. Ochalski, M. A. Morris, and J. D. Holmes, Non-equilibrium induction of tin in germanium: Towards direct bandgap  $Ge_{1-x}Sn_x$  nanowires, *Nat. Commun.* **7**, 11405 (2016).
- [35] S. Koelling, A. Li, A. Cavalli, S. Assali, D. Car, S. Gazibegovic, E. P. A. M. Bakkers, and P. M. Koenraad, Atom-by-Atom analysis of semiconductor nanowires with parts Per million sensitivity, *Nano Lett.* **17**, 599 (2017).
- [36] A. C. Meng, C. S. Fenrich, M. R. Braun, J. P. McVittie, A. F. Marshall, J. S. Harris, and P. C. McIntyre, Core/shell germanium/germanium-Tin nanowires exhibiting room temperature direct- and indirect-Gap photoluminescence, *Nano Lett.* **16**, 7521 (2016).
- [37] S. Assali, R. Bergamaschini, E. Scalise, M. A. Verheijen, M. Albani, A. Dijkstra, A. Li, S. Koelling, E. P. A. M. Bakkers, F. Montalenti, and L. Miglio, Kinetic control of morphology and composition in Ge/GeSn core/shell nanowires, *ACS Nano* **14**, 2445 (2020).
- [38] M. S. Seifner, A. Dijkstra, J. Bernardi, A. Steiger-Thirsfeld, M. Sistani, A. Lugstein, J. E. M. Haverkort, and S. Barth, Epitaxial  $Ge_{0.81}Sn_{0.19}$  nanowires for nanoscale Mid-infrared emitters, *ACS Nano* **13**, 8047 (2019).
- [39] É. Bouthillier, S. Assali, J. Nicolas, and O. Moutanabbir, Decoupling the effects of composition and strain on the vibrational modes of GeSn semiconductors, *Semicond. Sci. Technol.* **35**, 095006 (2020).
- [40] See Supplemental Material at <http://link.aps.org/supplemental/10.1103/PhysRevApplied.15.014034> for details of the experimental setup, top-down NW fabrication, FDTD simulation, and modal analysis, which includes Refs. [41–49].
- [41] H. G. Tompkins, E. A. Irene, I. An, H. Arwin, C. Chen, R. W. Collins, A. S. Ferlauto, J. N. Hilfiker, J. Humlíček, J. Gerald, E. Jellison, J. Lee, F. A. Modine, A. Röseler, M. Schubert, and J. A. Zapien, *Handbooks of Ellipsometry* (William Andrew Publishing And Springer-Verlag GmbH & Co. KG, Norwich, NY, 2005).
- [42] B. Johs, C. M. Herzinger, J. H. Dinan, A. Cornfeld, and J. Benson, Development of a parametric optical constant model for  $Hg_{1-x}Cd_xTe$  for control of composition by spectroscopic ellipsometry during MBE growth, *Thin Solid Films* **313–314**, 137 (1998).
- [43] D. E. Aspnes, Minimal-data approaches for determining outer-layer dielectric responses of films from kinetic reflectometric and ellipsometric measurements, *J. Opt. Soc. Am. A* **10**, 974 (1993).
- [44] S. D. Gedney, An anisotropic perfectly matched layer-absorbing medium for the truncation of FDTD lattices, *IEEE Trans. Antennas Propag.* **44**, 1630 (1996).
- [45] Y. Zhang and M. Loncar, Ultra-high quality factor optical resonators based on semiconductor nanowires, *Opt. Express* **16**, 17400 (2008).
- [46] B. Wang and P. W. Leu, Tunable and selective resonant absorption in vertical nanowires, *Opt. Lett.* **37**, 3756 (2012).
- [47] K. T. Fountaine, W. S. Whitney, and H. A. Atwater, Resonant absorption in semiconductor nanowires and nanowire arrays: Relating leaky waveguide modes to Bloch photonic crystal modes, *J. Appl. Phys.* **116**, 153106 (2014).

- [48] A. W. Snyder and J. Love, *Optical Waveguide Theory*, Vol. 2 (Springer-Verlag US, Boston, MA, 1983).
- [49] N. Anttu and H. Q. Xu, Efficient light management in vertical nanowire arrays for photovoltaics, *Opt. Express* **21**, A558 (2013).
- [50] N. Anttu, Absorption of light in a single vertical nanowire and a nanowire array, *Nanotechnology* **30**, 104004 (2019).
- [51] Y. Chen, M.-E. Pistol, and N. Anttu, Design for strong absorption in a nanowire array tandem solar cell, *Sci. Rep.* **6**, 32349 (2016).
- [52] J. A. Conway, S. Sahni, and T. Szkopek, Plasmonic interconnects versus conventional interconnects: A comparison of latency, crosstalk and energy costs, *Opt. Express* **15**, 4474 (2007).
- [53] J. Wallentin, N. Anttu, D. Asoli, M. Huffman, I. Aberg, M. H. Magnusson, G. Siefer, P. Fuss-Kailuweit, F. Dimroth, B. Witzigmann, H. Q. Xu, L. Samuelson, K. Deppert, and M. T. Borgstrom, InP nanowire array solar cells achieving 13.8% efficiency by exceeding the Ray optics limit, *Science (80-.)* **339**, 1057 (2013).
- [54] E. C. Garnett, M. L. Brongersma, Y. Cui, and M. D. McGehee, Nanowire solar cells, *Annu. Rev. Mater. Res.* **41**, 269 (2011).
- [55] J. Kupec, R. L. Stoop, and B. Witzigmann, Light absorption and emission in nanowire array solar cells, *Opt. Express* **18**, 27589 (2010).
- [56] P. M. Wu, N. Anttu, H. Q. Xu, L. Samuelson, and M. E. Pistol, Colorful InAs nanowire arrays: From strong to weak absorption with geometrical tuning, *Nano Lett.* **12**, 1990 (2012).
- [57] L. Hu and G. Chen, Analysis of optical absorption in silicon nanowire arrays for photovoltaic applications, *Nano Lett.* **7**, 3249 (2007).
- [58] J. Zhu, Z. Yu, G. F. Burkhardt, C. M. Hsu, S. T. Connor, Y. Xu, Q. Wang, M. McGehee, S. Fan, and Y. Cui, Optical absorption enhancement in amorphous silicon nanowire and nanocone arrays, *Nano Lett.* **9**, 279 (2009).
- [59] B. Wang, E. Stevens, and P. W. Leu, Strong broadband absorption in GaAs nanocone and nanowire arrays for solar cells, *Opt. Express* **22**, A386 (2014).
- [60] K. T. Fountaine, C. G. Kendall, and H. A. Atwater, Near-unity broadband absorption designs for semiconducting nanowire arrays via localized radial mode excitation, *Opt. Express* **22**, A930 (2014).
- [61] H. Lin, F. Xiu, M. Fang, S. Yip, H.-Y. Cheung, F. Wang, N. Han, K. S. Chan, C.-Y. Wong, and J. C. Ho, Rational design of inverted nanopencil arrays for cost-effective, broadband, and omnidirectional light harvesting, *ACS Nano* **8**, 3752 (2014).
- [62] L. Cao, J. S. White, J.-S. Park, J. a Schuller, B. M. Clemens, and M. L. Brongersma, Engineering light absorption in semiconductor nanowire devices, *Nat. Mater.* **8**, 643 (2009).
- [63] J. Kupec and B. Witzigmann, Dispersion, wave propagation and efficiency analysis of nanowire solar cells, *Opt. Express* **17**, 10399 (2009).
- [64] M. Ko, S. H. Baek, B. Song, J. W. Kang, S. A. Kim, and C. H. Cho, Periodically diameter-modulated semiconductor nanowires for enhanced optical absorption, *Adv. Mater.* **28**, 2504 (2016).
- [65] M. L. Brongersma, Y. Cui, and S. Fan, Light management for photovoltaics using high-index nanostructures, *Nat. Mater.* **13**, 451 (2014).
- [66] J. Yin, Y. Zang, C. Yue, X. He, J. Li, Z. Wu, and Y. Fang, Self-assembled hollow nanosphere arrays used as low Q whispering gallery mode resonators on thin film solar cells for light trapping, *Phys. Chem. Chem. Phys.* **15**, 16874 (2013).
- [67] J. Svensson, N. Anttu, N. Vainorius, B. M. Borg, and L.-E. Wernersson, Diameter-dependent photocurrent in InAsSb nanowire infrared photodetectors, *Nano Lett.* **13**, 1380 (2013).
- [68] Y. Yu and L. Cao, Coupled leaky mode theory for light absorption in 2D, 1D, and 0D semiconductor nanostructures, *Opt. Express* **20**, 13847 (2012).
- [69] A. Yariv, Universal relations for coupling of optical power between microresonators and dielectric waveguides, *Electron. Lett.* **36**, 321 (2000).
- [70] F. Gunning and B. Corbett, Time to open the 2- $\mu\text{m}$  window?, *Opt. Photonics News* **30**, 42 (2019).